

An energetically balanced, quasi-Newton integrator for non-hydrostatic vertical atmospheric dynamics

David Lee^{a,*}

^a*Department of Mechanical and Aerospace Engineering, Monash University, Melbourne 3800, Australia*

Abstract

An energetically balanced, implicit integrator for non-hydrostatic vertical atmospheric dynamics on the sphere is presented. The integrator allows for the exact balance of energy exchanges in space and time for vertical atmospheric motions by preserving the skew-symmetry of the non-canonical Hamiltonian formulation of the compressible Euler equations. Essential to the efficient implementation of such an integrator is a preconditioning strategy that reduces the dimensionality of the inner linear system. Here we reduce the four component velocity, density, density weighted potential temperature and Exner pressure system into a single equation for the density weighted potential temperature via repeated Schur complement decomposition and the careful selection of coupling terms. The integrator is validated for standard test cases of baroclinic stability and a non-hydrostatic gravity wave on the sphere, and shows robust convergence in both regimes.

Keywords: Poisson integrator, Non-hydrostatic, Euler equations, Cubed sphere, Horizontally explicit/vertically implicit, Quasi-Newton

1. Introduction

Energy conserving, semi-implicit time integrators for various geophysical systems in Hamiltonian form have been previously introduced for the shallow water [1, 3] and thermal shallow water [2, 4] equations on the sphere, and the compressible Euler equations in vertical slice geometry [4]. They have also been implemented on other areas, such as plasma physics [5]. These integrators are based on discrete gradient methods [6, 7] for non-canonical Hamiltonian systems which preserve the skew-symmetric property of the Poisson bracket in both the spatial and temporal discretisation. In doing so these integrators satisfy exact balances of energy exchanges, as well as the orthogonality of the vorticity dynamics to these energetic exchanges. By mitigating against internal biases in the representation of dynamical processes these integrators may help to improve the statistical quality of long time integrations.

In the present article a skew-symmetric mimetic spectral element spatial discretisation of the 3D compressible Euler equations on the sphere [8] is extended to incorporate such an integrator for non-hydrostatic vertical dynamics. The vertical integrator is coupled to the explicit horizontal dynamics using a trapezoidal horizontally explicit/vertically implicit (HEVI) splitting scheme [9, 10], which complements the centered time integration of the vertical scheme. Such schemes have previously been used as the basis for energy conserving spatial discretisations of vertical dynamics in non-hydrostatic atmospheric modelling [11]. In order to accelerate the performance of such an integrator, Schur complement reduction may be applied in order to transform the coupled system into a single equation at each linear solve [12, 13]. In the present formulation the coupled velocity, density, density weighted potential temperature, Exner pressure system is reduced to a single equation for the density weighted potential temperature, for which the implicit Helmholtz operator incorporates corrections to both the gradient and divergence operators in order to account for the thermodynamics. This operator is derived from the reduction of an approximate Jacobian for a deliberate choice of coupling terms.

*Corresponding author. Tel. +61 452 262 804.

Email address: davelee2804@gmail.com (David Lee)

In section 2 the 3D compressible Euler equations are introduced in continuous form, including a brief discussion of their energetic properties. Section 3 will briefly discuss the mixed mimetic spectral element spatial discretisation of the 3D compressible Euler equations [8]. For more extensive discussions of this discretisation [14, 15] and its properties for geophysical flow simulation [16, 17] the reader is referred to the aforementioned articles. Section 4 will discuss the formulation of the quasi-Newton vertical dynamics integrator, including the nonlinear preconditioning strategy. Results will be presented in section 5, and finally conclusions and discussion of future work will be presented in section 6.

2. The rotating 3D compressible Euler equations

The three dimensional compressible Euler equations for a shallow atmosphere may be expressed as [8, 18, 19]

$$\frac{\partial \mathbf{u}}{\partial t} + (\boldsymbol{\omega} + \mathbf{f}) \times \mathbf{u} + \nabla \left(\frac{1}{2} \|\mathbf{u}\|^2 + gz \right) + \theta \nabla \Pi = 0, \quad (1a)$$

$$\frac{\partial \rho}{\partial t} + \nabla \cdot (\rho \mathbf{u}) = 0, \quad (1b)$$

$$\frac{\partial \rho \theta}{\partial t} + \nabla \cdot (\rho \theta \mathbf{u}) = 0, \quad (1c)$$

where $\mathbf{u} = u\mathbf{e}_\lambda + v\mathbf{e}_\varphi + w\mathbf{e}_z$ are the zonal, meridional and vertical velocity components respectively, ρ is the density, $\mathbf{f} = f\mathbf{e}_z$ is the Coriolis term, g is the acceleration due to gravity, θ is the potential temperature, and Π is the Exner pressure (including the specific heat at constant pressure). The potential temperature and Exner pressure are defined with respect to the standard thermodynamic variables of temperature, T , and pressure, p , as

$$\Pi := c_p \left(\frac{p}{p_0} \right)^{\frac{R}{c_p}}, \quad (2a)$$

$$\theta := \frac{c_p T}{\Pi}, \quad (2b)$$

where c_p for the specific heat at constant pressure, p_0 is the reference pressure, and $R = c_p - c_v$ is the ideal gas constant (and c_v is the specific heat at constant volume). Using (2) the ideal gas law, $p = R\rho T$ may be reformulated as

$$\Pi = c_p \left(\frac{R\rho\theta}{p_0} \right)^{\frac{R}{c_v}}. \quad (3)$$

To obtain a closed system for the solution of the compressible Euler equations, (1) and (3) must be supplemented by appropriate boundary conditions. We impose homogeneous Dirichlet boundary conditions on the z -component of velocity, w as

$$w|_{z=0} = w|_{z=z^{\text{top}}} = 0, \quad (4)$$

where z^{top} corresponds to the z -coordinates of the top boundary of the domain. We also apply homogeneous Neumann boundary conditions on the Exner pressure as

$$\left. \frac{\partial \Pi}{\partial z} \right|_{z=0} = \left. \frac{\partial \Pi}{\partial z} \right|_{z=z^{\text{top}}} = 0. \quad (5)$$

Note that in this formulation we have invoked the shallow atmosphere approximation, for which gravity is constant throughout the fluid column, the height of the fluid column is negligible with respect to the earth's radius, and the horizontal components of the Coriolis term are omitted [20].

2.1. Energetics

In this section the energetics of with 3D compressible Euler equations will be briefly analysed. in continuous form. The energetics of the discrete formulation will be discussed in subsequent sections.

2.1.1. Kinetic, potential, and internal energy

The kinetic energy, K , is defined as

$$K := \frac{1}{2} \langle \mathbf{u}, \rho \mathbf{u} \rangle = \frac{1}{2} \int_{\Omega} \rho \|\mathbf{u}\|^2, \quad (6)$$

where $\|\mathbf{u}\| := \langle \mathbf{u}, \mathbf{u} \rangle$, and $\langle \cdot, \cdot \rangle$ is the L^2 inner product given for scalar fields as

$$\langle f, g \rangle := \int_{\Omega} f g \, d\Omega, \quad (7)$$

and for vector fields as

$$\langle \mathbf{u}, \mathbf{v} \rangle := \int_{\Omega} \mathbf{u} \cdot \mathbf{v} \, d\Omega. \quad (8)$$

The time variation of kinetic energy is obtained by summing the L^2 inner product, between the momentum equation, (1a), and $\rho \mathbf{u}$, and between the continuity equation, (1b), and $\frac{1}{2} \|\mathbf{u}\|^2$

$$\frac{\partial K}{\partial t} = -\langle g, \rho w \rangle - \langle \rho \mathbf{u}, \theta \nabla \Pi \rangle, \quad (9)$$

where again w is the z -component of the velocity field, \mathbf{u} .

The potential energy, P , is given by

$$P := \langle \rho, g z \rangle = \int_{\Omega} \rho g z \, d\Omega, \quad (10)$$

and its time derivative follows directly

$$\frac{\partial P}{\partial t} = \left\langle g z, \frac{\partial \rho}{\partial t} \right\rangle \stackrel{(1b)}{=} -\langle g z, \nabla \cdot (\rho \mathbf{u}) \rangle = \langle g, \rho w \rangle, \quad (11)$$

where we have used integration by parts on the last identity and assumed periodic boundary conditions in the horizontal directions, together with homogeneous boundary conditions for the vertical component of the velocity field, (4).

The internal energy, I , is defined as

$$I := \int_{\Omega} c_v \rho T \, d\Omega \stackrel{(2b)}{=} \int_{\Omega} \frac{c_v}{c_p} \rho \theta \Pi \, d\Omega = \int_{\Omega} c_v \rho \theta \left(\frac{R \rho \theta}{p_0} \right)^{\frac{R}{c_v}} \, d\Omega = \int_{\Omega} c_v \left(\frac{R}{p_0} \right)^{\frac{R}{c_v}} (\rho \theta)^{\frac{c_p}{c_v}} \, d\Omega. \quad (12)$$

After some manipulation, the time variation of internal energy is given by

$$\frac{\partial I}{\partial t} = -\langle \nabla \cdot (\rho \theta \mathbf{u}), \Pi \rangle = \langle \rho \mathbf{u}, \theta \nabla \Pi \rangle. \quad (13)$$

where integration by parts was used on the last identity, together with homogeneous boundary conditions for \mathbf{u} and periodic boundary conditions on the horizontal directions.

2.1.2. Conservation of total energy

Following [19], the total energy, \mathcal{H} , is given as the sum of kinetic, K , potential, P , and internal, I , energy as

$$\mathcal{H} := K + P + I = \int_{\Omega} \frac{1}{2} \rho u^2 \, d\Omega + \int_{\Omega} \rho g z \, d\Omega + \int_{\Omega} \frac{c_v}{c_p} \Theta \Pi \, d\Omega. \quad (14)$$

where $\Theta := \rho \theta$. The variational derivatives of \mathcal{H} with respect to the prognostic variables \mathbf{u} , ρ , and Θ , are given as

$$\frac{\delta \mathcal{H}}{\delta \mathbf{u}} = \rho \mathbf{u} = \mathbf{U}, \quad \frac{\delta \mathcal{H}}{\delta \rho} = \frac{1}{2} u^2 + g z = \Phi, \quad \frac{\delta \mathcal{H}}{\delta \Theta} = \Pi. \quad (15)$$

Writing the prognostic variables as a column vector of the form, $\mathbf{a} = [\mathbf{u} \quad \rho \quad \Theta]^\top$, we may then express the original system (1) as [21]

$$\frac{\partial \mathbf{a}}{\partial t} = \mathbf{B} \frac{\delta \mathcal{H}}{\delta \mathbf{a}}, \quad (16)$$

where \mathbf{B} is a skew-symmetric operator of the form

$$\mathbf{B} := \begin{bmatrix} -\mathbf{q} \times (\cdot) & -\nabla(\cdot) & -\theta \nabla(\cdot) \\ -\nabla \cdot (\cdot) & 0 & 0 \\ -\nabla \cdot (\theta \cdot) & 0 & 0 \end{bmatrix}, \quad (17)$$

and $\mathbf{q} = (\boldsymbol{\omega} + \mathbf{f})/\rho$ is the potential vorticity. Energy conservation is then assured since

$$\frac{\partial \mathcal{H}}{\partial t} = \frac{\delta \mathcal{H}}{\delta \mathbf{a}} \cdot \frac{\partial \mathbf{a}}{\partial t} \stackrel{(16)}{=} \frac{\delta \mathcal{H}}{\delta \mathbf{a}} \cdot \left(\mathbf{B} \frac{\delta \mathcal{H}}{\delta \mathbf{a}} \right) = 0, \quad (18)$$

where the last identity follows from the skew-symmetry of \mathbf{B} .

3. Spatial discretisation

In this section we briefly describe some of the important features of the mixed mimetic spectral element spatial discretisation used in this work. For a complete description of this discretisation as it applies to the 3D compressible Euler equations on the cubed sphere see [8].

The mixed mimetic spectral element method [14, 15] is a compatible family of finite element spaces. For finite dimensional polynomial spaces of the form $\mathcal{P}_h(\Omega) \subset H^1(\Omega)$, $\mathcal{W}_h(\Omega) \subset H(\text{curl}, \Omega)$, $\mathcal{U}_h(\Omega) \subset H(\text{div}, \Omega)$, and $\mathcal{Q}_h(\Omega) \subset L^2(\Omega)$ the discrete analogues of the differential operators satisfy a series of compatibility relations of the form

$$\mathbb{R} \longrightarrow \mathcal{P}_h(\Omega) \xrightarrow{\nabla} \mathcal{W}_h(\Omega) \xrightarrow{\nabla \times} \mathcal{U}_h(\Omega) \xrightarrow{\nabla \cdot} \mathcal{Q}_h(\Omega) \longrightarrow 0, \quad (19)$$

where the space $H^1(\Omega)$ represents square integrable functions over Ω whose gradient is also square integrable, $H(\text{curl}, \Omega)$ and $H(\text{div}, \Omega)$ contain square integrable vector fields over Ω with square integrable curl and divergence respectively, and the function space $L^2(\Omega)$ contains square integrable functions. Each of these polynomial function spaces has an associated finite set of basis functions $\epsilon_i^{\mathcal{P}}$, $\epsilon_i^{\mathcal{W}}$, $\epsilon_i^{\mathcal{U}}$, and $\epsilon_i^{\mathcal{Q}}$, such that

$$\mathcal{P}_h = \text{span}\{\epsilon_1^{\mathcal{P}}, \dots, \epsilon_{d_p}^{\mathcal{P}}\}, \quad \mathcal{W}_h = \text{span}\{\epsilon_1^{\mathcal{W}}, \dots, \epsilon_{d_w}^{\mathcal{W}}\}, \quad \mathcal{U}_h = \text{span}\{\epsilon_1^{\mathcal{U}}, \dots, \epsilon_{d_u}^{\mathcal{U}}\}, \quad \text{and} \quad \mathcal{Q}_h = \text{span}\{\epsilon_1^{\mathcal{Q}}, \dots, \epsilon_{d_q}^{\mathcal{Q}}\}. \quad (20)$$

The discrete mappings given in (19) are represented by strong form topological relations as [14]:

$$\nabla \epsilon_j^{\mathcal{P}} = \sum_{k=0}^{d_Q} \mathbf{E}_{k,j}^{1,0} \epsilon_k^{\mathcal{W}}, \quad \nabla \times \epsilon_j^{\mathcal{W}} = \sum_{k=0}^{d_U} \mathbf{E}_{k,j}^{2,1} \epsilon_k^{\mathcal{U}}, \quad \text{and} \quad \nabla \cdot \epsilon_j^{\mathcal{U}} = \sum_{k=0}^{d_Q} \mathbf{E}_{k,j}^{3,2} \epsilon_k^{\mathcal{Q}}, \quad (21)$$

where $\mathbf{E}^{1,0}$, $\mathbf{E}^{2,1}$, and $\mathbf{E}^{3,2}$ are so called *incidence* matrices corresponding to the discrete versions of the differential operators grad, curl and div. Conversely, reverse mappings may be applied through weak form adjoints to these operators [15].

3.1. Directional splitting

Here we briefly describe the splitting procedure used to decompose the three dimensional problem into horizontal (two dimensional) and vertical sub-problems. Due to the nature of the various function spaces, this splitting implies no additional approximation to the spatial discretisation. However this construction does involve a temporal approximation, by which the horizontal and vertical sub problems are solved explicitly and implicitly respectively [9, 10].

We defined the horizontal, \mathbf{u}_{\parallel} , and vertical, \mathbf{u}_{\perp} , components of the velocity field $\mathbf{u} = u\mathbf{e}_x + v\mathbf{e}_y + w\mathbf{e}_z$

$$\mathbf{u}_{\parallel} := u\mathbf{e}_x + v\mathbf{e}_y, \quad \mathbf{u}_{\perp} := w\mathbf{e}_z. \quad (22)$$

Moreover, let ∇_{\parallel} and ∇_{\perp} represent the horizontal and vertical components of the gradient operator of a scalar field ρ

$$\nabla_{\parallel}\rho := \frac{1}{r\cos(\phi)}\frac{\partial\rho}{\partial\lambda}\mathbf{e}_{\lambda} + \frac{1}{r}\frac{\partial\rho}{\partial\phi}\mathbf{e}_{\phi}, \quad \nabla_{\perp}\rho := \frac{\partial\rho}{\partial z}\mathbf{e}_z. \quad (23)$$

In a similar way, $\nabla_{\parallel}\times$ and $\nabla_{\perp}\times$ represent, respectively, the horizontal and vertical components of the curl of a vector field $\mathbf{u} = u\mathbf{e}_{\lambda} + v\mathbf{e}_{\phi} + w\mathbf{e}_z$

$$\nabla_{\parallel}\times\mathbf{u} := \left(\frac{1}{r}\frac{\partial w}{\partial\phi} - \frac{\partial v}{\partial z}\right)\mathbf{e}_{\lambda} + \left(\frac{\partial u}{\partial z} - \frac{1}{r\cos(\phi)}\frac{\partial w}{\partial\lambda}\right)\mathbf{e}_{\phi}, \quad \nabla_{\perp}\times\mathbf{u} := \frac{1}{r\cos(\phi)}\left(\frac{\partial v}{\partial\lambda} - \frac{\partial(\cos(\phi)u)}{\partial\phi}\right)\mathbf{e}_z. \quad (24)$$

Note that we have assumed the shallow atmosphere approximation of constant radius, r , in the above expressions. In practice, these spherical transformations are absorbed into the definition of the Jacobian [22] and the associated Piola transformations for the different function spaces [8, 17].

From (23) and (24) follows directly that

$$\nabla\rho = \nabla_{\parallel}\rho + \nabla_{\perp}\rho, \quad \text{and} \quad \nabla\times\mathbf{u} = \nabla_{\parallel}\times\mathbf{u} + \nabla_{\perp}\times\mathbf{u}.$$

With (22) and (24) it is possible to rewrite the definition of vorticity, $\boldsymbol{\omega} := \nabla\times\mathbf{u}$, as

$$\boldsymbol{\omega} = \underbrace{\nabla_{\parallel}\times\mathbf{u}_{\parallel} + \nabla_{\parallel}\times\mathbf{u}_{\perp}}_{\boldsymbol{\omega}_{\parallel}} + \underbrace{\nabla_{\perp}\times\mathbf{u}_{\parallel}}_{\boldsymbol{\omega}_{\perp}}. \quad (25)$$

While the spatial discretisation outlined above is valid for basis functions of any polynomial degree, p , in practice we use polynomials of arbitrary order in the horizontal only, and use a lowest order discretisation in the vertical for which the \mathcal{P}_h bases are piecewise linear and the \mathcal{Q}_h bases are piecewise constant [8].

Using (22), (23), (24), and (25), we may split the compressible Euler equations, (1), into horizontal and vertical components

$$\frac{\partial\mathbf{u}_{\parallel}}{\partial t} + (\boldsymbol{\omega}_{\perp} + \mathbf{f}_{\perp})\times\mathbf{u}_{\parallel} + \boldsymbol{\omega}_{\parallel,\parallel}\times\mathbf{u}_{\perp} + \frac{1}{2}\nabla_{\parallel}\|\mathbf{u}_{\parallel}\|^2 + \theta\nabla_{\parallel}\Pi = 0, \quad (26a)$$

$$\frac{\partial\mathbf{u}_{\perp}}{\partial t} + \boldsymbol{\omega}_{\parallel,\perp}\times\mathbf{u}_{\parallel} + \nabla_{\perp}\left(\frac{1}{2}\|\mathbf{u}_{\perp}\|^2 + gz\right) + \theta\nabla_{\perp}\Pi = 0, \quad (26b)$$

$$\frac{\partial\rho}{\partial t} + \nabla\cdot(\rho\mathbf{u}_{\parallel}) + \nabla\cdot(\rho\mathbf{u}_{\perp}) = 0, \quad (26c)$$

$$\frac{\partial(\rho\theta)}{\partial t} + \nabla\cdot(\rho\theta\mathbf{u}_{\parallel}) + \nabla\cdot(\rho\theta\mathbf{u}_{\perp}) = 0, \quad (26d)$$

where, as in (25), $\boldsymbol{\omega}_{\parallel,\parallel} := \nabla_{\parallel}\times\mathbf{u}_{\parallel}$ and $\boldsymbol{\omega}_{\parallel,\perp} := \nabla_{\parallel}\times\mathbf{u}_{\perp}$. The same splitting into horizontal and vertical components may be applied for the basis functions, (20),

$$\boldsymbol{\epsilon}_j^{\mathcal{W}} = (\boldsymbol{\epsilon}_j^{\mathcal{W}})_{\parallel} + (\boldsymbol{\epsilon}_j^{\mathcal{W}})_{\perp} := \boldsymbol{\epsilon}_j^{\mathcal{W}_{\parallel}} + \boldsymbol{\epsilon}_j^{\mathcal{W}_{\perp}}, \quad (27)$$

and

$$\boldsymbol{\epsilon}_j^{\mathcal{U}} = (\boldsymbol{\epsilon}_j^{\mathcal{U}})_{\parallel} + (\boldsymbol{\epsilon}_j^{\mathcal{U}})_{\perp} := \boldsymbol{\epsilon}_j^{\mathcal{U}_{\parallel}} + \boldsymbol{\epsilon}_j^{\mathcal{U}_{\perp}}. \quad (28)$$

Multiplying each of these equations by the appropriate finite dimensional test functions, and discretising the

solution variables accordingly, the horizontal discrete equations are given as [8]

$$\begin{aligned}
& \sum_{i=0}^{d_{\mathcal{U}_{\parallel}}-1} \langle \epsilon_j^{\mathcal{U}_{\parallel}}, \epsilon_i^{\mathcal{U}_{\parallel}} \rangle_{\Omega} \frac{du_{i,\parallel}}{dt} + \sum_{i=0}^{d_{\mathcal{U}_{\parallel}}-1} \langle \epsilon_j^{\mathcal{U}_{\parallel}}, (\omega_{h,\perp} + f_{h,\perp}) \times \epsilon_i^{\mathcal{U}_{\parallel}} \rangle_{\Omega} u_{i,\parallel} + \\
& \sum_{i=0}^{d_{\mathcal{U}_{\perp}}-1} \langle \epsilon_j^{\mathcal{U}_{\parallel}}, \omega_{h,\parallel,\parallel} \times \epsilon_i^{\mathcal{U}_{\perp}} \rangle_{\Omega} u_{i,\perp} + \\
& \sum_{i,k=0}^{d_Q-1, d_Q-1} (\mathbb{E}_{\parallel}^{3,2})_{j,k}^{\top} \left\langle \epsilon_k^Q, \frac{1}{2} \mathbf{u}_{h,\parallel} \cdot \epsilon_i^{\mathcal{U}_{\parallel}} \right\rangle_{\Omega} u_{i,\parallel} +
\end{aligned} \tag{29a}$$

$$\begin{aligned}
& \sum_{i=0}^{d_{\mathcal{U}_{\parallel}}-1} \langle \epsilon_j^{\mathcal{U}_{\parallel}}, \theta_h \epsilon_i^{\mathcal{U}_{\parallel}} \rangle_{\Omega} P_{i,\parallel} = 0, \quad j = 0, \dots, d_{\mathcal{U}_{\parallel}} - 1, \\
& \sum_{i,k=0}^{d_Q-1, d_Q-1} (\mathbb{E}_{\parallel}^{3,2})_{j,k}^{\top} \langle \epsilon_k^Q, \epsilon_i^Q \rangle_{\Omega} \Pi_i - \sum_{i=0}^{d_{\mathcal{U}_{\parallel}}-1} \langle \epsilon_j^{\mathcal{U}_{\parallel}}, \epsilon_i^{\mathcal{U}_{\parallel}} \rangle_{\Omega} P_{i,\parallel} = 0, \quad j = 0, \dots, d_{\mathcal{U}_{\parallel}} - 1
\end{aligned} \tag{29b}$$

$$\sum_{i=0}^{d_{\mathcal{U}_{\parallel}}-1} \langle \epsilon_j^{\mathcal{U}_{\parallel}}, \rho_h \epsilon_i^{\mathcal{U}_{\parallel}} \rangle_{\Omega} u_{i,\parallel} - \sum_{i=0}^{d_{\mathcal{U}_{\parallel}}-1} \langle \epsilon_j^{\mathcal{U}_{\parallel}}, \epsilon_i^{\mathcal{U}_{\parallel}} \rangle_{\Omega} u_{i,\parallel} = 0, \quad j = 0, \dots, d_{\mathcal{U}_{\parallel}} - 1, \tag{29c}$$

$$\sum_{i=0}^{d_{\mathcal{U}_{\parallel}}-1} \langle \epsilon_j^{\mathcal{U}_{\parallel}}, \theta_h \epsilon_i^{\mathcal{U}_{\parallel}} \rangle_{\Omega} u_{i,\parallel} - \sum_{i=0}^{d_{\mathcal{U}_{\parallel}}-1} \langle \epsilon_j^{\mathcal{U}_{\parallel}}, \epsilon_i^{\mathcal{U}_{\parallel}} \rangle_{\Omega} F_{i,\parallel} = 0, \quad j = 0, \dots, d_{\mathcal{U}_{\parallel}} - 1, \tag{29d}$$

$$\sum_{i,k=0}^{d_{\mathcal{U}_{\parallel}}-1, d_{\mathcal{U}_{\parallel}}-1} (\mathbb{E}_{\parallel,\parallel}^{2,1})_{j,k}^{\top} \langle \epsilon_k^{\mathcal{U}_{\parallel}}, \epsilon_i^{\mathcal{U}_{\parallel}} \rangle_{\Omega} u_{i,\parallel} - \sum_{i=0}^{d_{\mathcal{W}_{\parallel}}-1} \langle \epsilon_j^{\mathcal{W}_{\parallel}}, \epsilon_i^{\mathcal{W}_{\parallel}} \rangle_{\Omega} \omega_{i,\parallel,\parallel} = 0, \quad j = 0, \dots, d_{\mathcal{W}_{\parallel}} - 1, \tag{29e}$$

$$\sum_{i,k=0}^{d_{\mathcal{U}_{\parallel}}-1, d_{\mathcal{U}_{\parallel}}-1} (\mathbb{E}_{\parallel,\perp}^{2,1})_{j,k}^{\top} \langle \epsilon_k^{\mathcal{U}_{\parallel}}, \epsilon_i^{\mathcal{U}_{\parallel}} \rangle_{\Omega} u_{i,\parallel} - \sum_{i=0}^{d_{\mathcal{W}_{\perp}}-1} \langle \epsilon_j^{\mathcal{W}_{\perp}}, \epsilon_i^{\mathcal{W}_{\perp}} \rangle_{\Omega} \omega_{i,\perp} = 0, \quad j = 0, \dots, d_{\mathcal{W}_{\perp}} - 1, \tag{29f}$$

where we have introduced $\omega_{h,\parallel,\parallel} := \sum_{i=0}^{d_{\mathcal{W}_{\parallel}}-1} \omega_{i,\parallel,\parallel} \epsilon_i^{\mathcal{W}_{\parallel}}$, $\omega_{h,\parallel,\perp} := \sum_{i=0}^{d_{\mathcal{W}_{\perp}}-1} \omega_{i,\parallel,\perp} \epsilon_i^{\mathcal{W}_{\parallel}}$. Note that we have introduced additional diagnostic equations for the pressure gradients (29b), mass and temperature fluxes, (29c), (29d) and vorticity

terms, (29e), (29f). In the same way, the vertical discrete equations are

$$\sum_{i=0}^{d_{u_{\perp}}-1} \langle \epsilon_j^{\mathcal{U}_{\perp}}, \epsilon_i^{\mathcal{U}_{\perp}} \rangle_{\Omega} \frac{du_{i,\perp}}{dt} + \sum_{i=0}^{d_{u_{\parallel}}-1} \langle \epsilon_j^{\mathcal{U}_{\perp}}, \omega_{h,\parallel,\perp} \times \epsilon_i^{\mathcal{U}_{\parallel}} \rangle_{\Omega} u_{i,\parallel} + \sum_{i,k=0}^{d_Q-1, d_Q-1} (\mathbf{E}_{\perp}^{3,2})_{j,k}^{\top} \left\langle \epsilon_k^Q, \frac{1}{2} \mathbf{u}_{h,\perp} \cdot \epsilon_i^{\mathcal{U}_{\perp}} \right\rangle_{\Omega} u_{i,\perp} + \quad (30a)$$

$$\sum_{i,k=0}^{d_Q-1, d_Q-1} g (\mathbf{E}_{\perp}^{3,2})_{j,k}^{\top} \langle \epsilon_k^Q, \epsilon_i^Q \rangle_{\Omega} z_i + \sum_{i=0}^{d_{u_{\perp}}-1} \langle \epsilon_j^{\mathcal{U}_{\perp}}, \theta_h \epsilon_i^{\mathcal{U}_{\perp}} \rangle_{\Omega} P_{i,\perp} = 0, \quad j = 0, \dots, d_{u_{\perp}} - 1,$$

$$\sum_{i,k=0}^{d_Q-1, d_Q-1} (\mathbf{E}_{\perp}^{3,2})_{j,k}^{\top} \langle \epsilon_j^Q, \epsilon_i^Q \rangle_{\Omega} \Pi_i - \sum_{i=0}^{d_{u_{\perp}}-1} \langle \epsilon_j^{\mathcal{U}_{\perp}}, \epsilon_i^{\mathcal{U}_{\perp}} \rangle_{\Omega} P_{i,\perp} = 0, \quad j = 0, \dots, d_{u_{\perp}} - 1 \quad (30b)$$

$$\sum_{i=0}^{d_{u_{\perp}}-1} \langle \epsilon_j^{\mathcal{U}_{\perp}}, \rho_h \epsilon_i^{\mathcal{U}_{\perp}} \rangle_{\Omega} u_{i,\perp} - \sum_{i=0}^{d_{u_{\perp}}-1} \langle \epsilon_j^{\mathcal{U}_{\perp}}, \epsilon_i^{\mathcal{U}_{\perp}} \rangle_{\Omega} U_{i,\perp} = 0, \quad j = 0, \dots, d_{u_{\perp}} - 1, \quad (30c)$$

$$\sum_{i=0}^{d_{u_{\perp}}-1} \langle \epsilon_j^{\mathcal{U}_{\perp}}, \theta_h \epsilon_i^{\mathcal{U}_{\perp}} \rangle_{\Omega} U_{i,\perp} - \sum_{i=0}^{d_{u_{\perp}}-1} \langle \epsilon_j^{\mathcal{U}_{\perp}}, \epsilon_i^{\mathcal{U}_{\perp}} \rangle_{\Omega} F_{i,\perp} = 0, \quad j = 0, \dots, d_{u_{\perp}} - 1, \quad (30d)$$

$$\sum_{i,k=0}^{d_{u_{\perp}}-1, d_{u_{\perp}}-1} (\mathbf{E}_{\perp}^{2,1})_{j,k}^{\top} \langle \epsilon_k^{\mathcal{U}_{\perp}}, \epsilon_i^{\mathcal{U}_{\perp}} \rangle_{\Omega} u_{i,\perp} - \sum_{i=0}^{d_{w_{\parallel}}-1} \langle \epsilon_j^{\mathcal{W}_{\parallel}}, \epsilon_i^{\mathcal{W}_{\parallel}} \rangle_{\Omega} \omega_{i,\parallel,\perp} = 0, \quad j = 0, \dots, d_{w_{\parallel}} - 1, \quad (30e)$$

where we have introduced $\omega_{h,\perp} := \sum_{i=0}^{d_{w_{\perp}}-1} \omega_{i,\perp} \epsilon_i^{\mathcal{W}_{\perp}}$.

Additionally, we also have the flux form equations for density and density weighted potential temperature transport that contain both vertical and horizontal components. While we have not included these in the split systems described in (29) and (30), since doing so incurs a temporal splitting error, in practice these equations are also split between their horizontal and vertical components. These equations are given as

$$\sum_{i=0}^{d_Q-1} \langle \epsilon_j^Q, \epsilon_i^Q \rangle_{\Omega} \frac{d\rho_i}{dt} + \sum_{i,k=0}^{d_{u_{\parallel}}-1, d_Q-1} \langle \epsilon_j^Q, \epsilon_k^Q \rangle_{\Omega} (\mathbf{E}_{\parallel}^{3,2})_{k,i} U_{i,\parallel} + \sum_{i,k=0}^{d_{u_{\perp}}-1, d_Q-1} \langle \epsilon_j^Q, \epsilon_k^Q \rangle_{\Omega} (\mathbf{E}_{\perp}^{3,2})_{k,i} U_{i,\perp} = 0, \quad j = 0, \dots, d_Q - 1 \quad (31a)$$

$$\sum_{i=0}^{d_Q-1} \langle \epsilon_j^Q, \epsilon_i^Q \rangle_{\Omega} \frac{d\Theta_i}{dt} + \sum_{i,k=0}^{d_{u_{\parallel}}-1, d_Q-1} \langle \epsilon_j^Q, \epsilon_k^Q \rangle_{\Omega} (\mathbf{E}_{\parallel}^{3,2})_{k,i} F_{i,\parallel} + \sum_{i,k=0}^{d_{u_{\perp}}-1, d_Q-1} \langle \epsilon_j^Q, \epsilon_k^Q \rangle_{\Omega} (\mathbf{E}_{\perp}^{3,2})_{k,i} F_{i,\perp} = 0, \quad j = 0, \dots, d_Q - 1, \quad (31b)$$

We also have two additional diagnostic equations for the potential temperature and Exner pressure. These are given respectively as

$$\sum_{i=0}^{d_Q-1} \langle \epsilon_j^{\mathcal{U}_{\perp}}, \epsilon_i^Q \rangle_{\Omega} \Theta_i - \sum_{i=0}^{d_{u_{\perp}}-1} \langle \epsilon_j^{\mathcal{U}_{\perp}}, \rho_h \epsilon_i^{\mathcal{U}_{\perp}} \rangle_{\Omega} \theta_i = 0, \quad j = 0, \dots, d_{u_{\perp}} - 1, \quad (32)$$

$$c_p \left(\frac{R}{p_0} \right)^{R/c_v} \sum_{i=0}^{d_{u_{\perp}}-1} \langle \epsilon_j^Q, (\epsilon_i^Q \Theta_i)^{R/c_v} \rangle_{\Omega} - \sum_{i=0}^{d_Q-1} \langle \epsilon_j^Q, \epsilon_i^Q \rangle_{\Omega} \Pi_i = 0, \quad j = 0, \dots, d_Q - 1. \quad (33)$$

For the sake of brevity, we use compact matrix notation for the remainder of this article. Using this notation, the horizontal system, (29) is expressed

$$\mathbf{M}^{\mathcal{U}_{\parallel}} \frac{d\mathbf{u}^{\parallel}}{dt} + \mathbf{R}^{\parallel,\parallel} \mathbf{u}^{\parallel} + \mathbf{R}^{\parallel,\perp} \mathbf{u}^{\perp} + (\mathbf{E}_{\parallel}^{3,2})^{\top} \mathbf{T}^{\mathcal{U}_{\parallel}} \mathbf{u}^{\parallel} + \mathbf{S}^{\mathcal{U}_{\parallel}} \mathbf{P}^{\parallel} = \mathbf{0}, \quad (34a)$$

$$(\mathbf{E}_{\parallel}^{3,2})^{\top} \mathbf{M}^Q \mathbf{\Pi} - \mathbf{M}^{\mathcal{U}_{\parallel}} \mathbf{P}^{\parallel} = \mathbf{0}, \quad (34b)$$

$$\mathbf{N}^{\mathcal{U}_{\parallel}} \mathbf{u}^{\parallel} - \mathbf{M}^{\mathcal{U}_{\parallel}} \mathbf{U}^{\parallel} = \mathbf{0}, \quad (34c)$$

$$\mathbf{S}^{\mathcal{U}_{\parallel}} \mathbf{U}^{\parallel} - \mathbf{M}^{\mathcal{U}_{\parallel}} \mathbf{F}^{\parallel} = \mathbf{0}, \quad (34d)$$

$$(\mathbf{E}_{\parallel,\parallel}^{2,1})^{\top} \mathbf{M}^{\mathcal{U}_{\parallel}} \mathbf{u}^{\parallel} - \mathbf{M}^{\mathcal{W}_{\parallel}} \omega^{\parallel,\parallel} = \mathbf{0}, \quad (34e)$$

$$(\mathbf{E}_{\perp}^{2,1})^{\top} \mathbf{M}^{\mathcal{U}_{\perp}} \mathbf{u}^{\perp} - \mathbf{M}^{\mathcal{W}_{\perp}} \omega^{\parallel,\perp} = \mathbf{0}. \quad (34f)$$

In a similar fashion, the discrete vertical equations, (30), are expressed as

$$\mathbf{M}^{\mathcal{U}_{\perp}} \frac{d\mathbf{u}^{\perp}}{dt} + \mathbf{R}^{\perp,\parallel} \mathbf{u}^{\parallel} + (\mathbf{E}_{\perp}^{3,2})^{\top} \mathbf{T}^{\mathcal{U}_{\perp}} \mathbf{u}^{\perp} + g (\mathbf{E}_{\perp}^{3,2})^{\top} \mathbf{M}^Q \mathbf{z} + \mathbf{S}^{\mathcal{U}_{\perp}} \mathbf{P}^{\perp} = \mathbf{0}, \quad (35a)$$

$$(\mathbf{E}_{\perp}^{3,2})^{\top} \mathbf{M}^Q \mathbf{\Pi} - \mathbf{M}^{\mathcal{U}_{\perp}} \mathbf{P}^{\perp} = \mathbf{0}, \quad (35b)$$

$$\mathbf{N}^{\mathcal{U}_{\perp}} \mathbf{u}^{\perp} - \mathbf{M}^{\mathcal{U}_{\perp}} \mathbf{U}^{\perp} = \mathbf{0}, \quad (35c)$$

$$\mathbf{S}^{\mathcal{U}_{\perp}} \mathbf{U}^{\perp} - \mathbf{M}^{\mathcal{U}_{\perp}} \mathbf{F}^{\perp} = \mathbf{0}, \quad (35d)$$

$$(\mathbf{E}_{\parallel,\perp}^{2,1})^{\top} \mathbf{M}^{\mathcal{U}_{\perp}} \mathbf{u}^{\perp} - \mathbf{M}^{\mathcal{W}_{\perp}} \omega^{\perp} = \mathbf{0}. \quad (35e)$$

Finally, (31)-(33) may be written in compact matrix notation as

$$\mathbf{M}^Q \frac{d\rho}{dt} + \mathbf{M}^Q \mathbf{E}_{\parallel}^{3,2} \mathbf{U}^{\parallel} + \mathbf{M}^Q \mathbf{E}_{\perp}^{3,2} \mathbf{U}^{\perp} = \mathbf{0}, \quad (36a)$$

$$\mathbf{M}^Q \frac{d\Theta}{dt} + \mathbf{M}^Q \mathbf{E}_{\parallel}^{3,2} \mathbf{F}^{\parallel} + \mathbf{M}^Q \mathbf{E}_{\perp}^{3,2} \mathbf{F}^{\perp} = \mathbf{0}, \quad (36b)$$

$$\mathbf{L}^{\mathcal{U}_{\perp},Q} \Theta - \mathbf{N}^{\mathcal{U}_{\perp}} \theta = \mathbf{0}, \quad (36c)$$

$$c_p \left(\frac{R}{p_0} \right)^{R/c_v} \sum_{i=0}^{d_{\mathcal{U}}-1} \langle \epsilon_j^Q, (\epsilon_i^Q \Theta_i)^{R/c_v} \rangle_{\Omega} - \mathbf{M}^Q \mathbf{\Pi} = \mathbf{0}. \quad (36d)$$

3.2. Discrete energetics

The discrete Hamiltonian $\mathcal{H}_h := \mathcal{H}[\mathbf{u}_h, \rho_h, \Theta_h]$ is given as [8]

$$\mathcal{H}[\mathbf{u}_h, \rho_h, \Theta_h] = \int_{\Omega} \frac{1}{2} \rho_h \|\mathbf{u}_h\|^2 d\Omega + \int_{\Omega} \rho_h g z_h d\Omega + \int_{\Omega} c_v \left(\frac{R}{p_0} \right)^{\frac{R}{c_v}} \Theta_h^{\frac{c_p}{c_v}} d\Omega. \quad (37)$$

Using the definition of the variational derivative [23], the variational derivatives of the Hamiltonian are given as

$$\left\langle \epsilon_j^{\mathcal{U}}, \frac{\delta \mathcal{H}}{\delta \mathbf{u}_h} \right\rangle = \left\langle \epsilon_j^{\mathcal{U}}, \rho_h \mathbf{u}_h \right\rangle = \left\langle \epsilon_j^{\mathcal{U}}, \mathbf{U}_h \right\rangle, \quad j = 0, \dots, d_{\mathcal{U}} \quad (38a)$$

$$\left\langle \epsilon_j^Q, \frac{\delta \mathcal{H}}{\delta \rho_h} \right\rangle = \left\langle \epsilon_j^Q, \frac{1}{2} \|\mathbf{u}_h\|^2 + g z_h \right\rangle = \left\langle \epsilon_j^Q, \Phi_h \right\rangle, \quad j = 0, \dots, d_Q \quad (38b)$$

$$\left\langle \epsilon_j^Q, \frac{\delta \mathcal{H}}{\delta \Theta_h} \right\rangle = c_p \left(\frac{R}{p_0} \right)^{R/c_v} \left\langle \epsilon_j^Q, \Theta_h^{R/c_v} \right\rangle = \left\langle \epsilon_j^Q, \Pi_h \right\rangle, \quad j = 0, \dots, d_Q. \quad (38c)$$

The semi-discrete form of the compressible Euler equations may then be formulated as a skew-symmetric system as

$$\begin{bmatrix} \mathbf{M}^{\mathcal{U}} \mathbf{u}_{,t} \\ \mathbf{M}^Q \rho_{,t} \\ \mathbf{M}^Q \Theta_{,t} \end{bmatrix} = \begin{bmatrix} -\mathbf{R}_q & (\mathbf{E}^{3,2})^{\top} \mathbf{M}^Q & \mathbf{S}^{\mathcal{U}} (\mathbf{M}^{\mathcal{U}})^{-1} (\mathbf{E}^{3,2})^{\top} \mathbf{M}^Q \\ -\mathbf{M}^Q \mathbf{E}^{3,2} & \mathbf{0} & \mathbf{0} \\ -\mathbf{M}^Q \mathbf{E}^{3,2} (\mathbf{M}^{\mathcal{U}})^{-1} \mathbf{S}^{\mathcal{U}} & \mathbf{0} & \mathbf{0} \end{bmatrix} \begin{bmatrix} \mathbf{U} \\ \Phi \\ \Pi \end{bmatrix}. \quad (39)$$

The fully discrete form of (39) is then given as

$$\begin{bmatrix} \mathbf{M}^u \mathbf{u}^{n+1} \\ \mathbf{M}^Q \rho^{n+1} \\ \mathbf{M}^Q \Theta^{n+1} \end{bmatrix} = \begin{bmatrix} \mathbf{M}^u \mathbf{u}^n \\ \mathbf{M}^Q \rho^n \\ \mathbf{M}^Q \Theta^n \end{bmatrix} + \Delta t \begin{bmatrix} -\widehat{\mathbf{R}}_q & (\mathbf{E}^{3,2})^\top \mathbf{M}^Q \widehat{\mathbf{S}}^u (\mathbf{M}^u)^{-1} (\mathbf{E}^{3,2})^\top \mathbf{M}^Q & 0 \\ -\mathbf{M}^Q \mathbf{E}^{3,2} & 0 & 0 \\ -\mathbf{M}^Q \mathbf{E}^{3,2} (\mathbf{M}^u)^{-1} \widehat{\mathbf{S}}^u & 0 & 0 \end{bmatrix} \begin{bmatrix} \bar{\mathbf{U}} \\ \bar{\Phi} \\ \bar{\Pi} \end{bmatrix}, \quad (40)$$

where $\widehat{\mathbf{R}}_q$ and $\widehat{\mathbf{S}}^u$ are time centered operators and $\bar{\mathbf{U}}$, $\bar{\Phi}$ and $\bar{\Pi}$ are second order in time versions of the variational derivatives of energy to be described in the next section. Multiplying both sides by $[\bar{\mathbf{U}}^\top \quad \bar{\Phi}^\top \quad \bar{\Pi}^\top]$, gives

$$\bar{\mathbf{U}}^\top \mathbf{M}^u (\mathbf{u}^{n+1} - \mathbf{u}^n) + \bar{\mathbf{U}}^\top (\mathbf{T}^u)^\top (\rho^{n+1} - \rho^n) + g \mathbf{z}^\top \mathbf{M}^Q (\rho^{n+1} - \rho^n) + \bar{\Pi}^\top \mathbf{M}^Q (\Theta^{n+1} - \Theta^n) = 0 \quad (41)$$

Note that for $\mathbf{R}_{q,ij} := \langle \epsilon_i^u, \mathbf{q}_h \times \epsilon_j^u \rangle_\Omega$, where \mathbf{q}_h is the potential vorticity [16], this is itself a skew-symmetric operator such that $\mathbf{U}^\top \mathbf{R}_q \mathbf{U} = \mathbf{U}^\top \mathbf{R} \mathbf{U} = \mathbf{0}$. As such neither \mathbf{R}_q nor \mathbf{R} projects onto the energy in the discrete form. Equation (41) is the discrete equivalent of (18), and ensures that total energy is conserved between time levels n and $n + 1$. This is achieved by the balanced exchanges of kinetic, potential and internal energy, which are given as

$$\frac{\partial K_h}{\partial t} = g \bar{\mathbf{U}}^\top (\mathbf{E}^{3,2})^\top \mathbf{M}^Q \mathbf{z} + \bar{\mathbf{U}}^\top \widehat{\mathbf{S}}^u (\mathbf{M}^u)^{-1} (\mathbf{E}^{3,2})^\top \mathbf{M}^Q \bar{\Pi}, \quad (42)$$

$$\frac{\partial P_h}{\partial t} = -g \mathbf{z}^\top \mathbf{M}^Q \mathbf{E}^{3,2} \bar{\mathbf{U}}, \quad (43)$$

$$\frac{\partial I_h}{\partial t} = -\bar{\Pi}^\top \mathbf{M}^Q \mathbf{E}^{3,2} (\mathbf{M}^u)^{-1} \widehat{\mathbf{S}}^u \bar{\mathbf{U}}. \quad (44)$$

The right hand side terms of (42) exactly balance those of (43) and (44), thus allowing for the exact balances of kinetic to potential and kinetic to internal energy respectively.

4. Temporal discretisation

The horizontal and vertical spatial discretisations described above (34)-(36) are time split using a horizontally explicit/vertically implicit (HEVI) scheme. While implicit vertical solvers are traditionally used in order to time step over the CFL limit of the vertical acoustic modes, here we have the additional motivation of conserving energetic exchanges associated with vertical atmospheric processes. Various flavors of HEVI schemes have previously been employed in non-hydrostatic atmospheric models [24–27]. The specific HEVI splitting used here is the horizontally third order, vertically second order, TRAP(2,3,2) scheme [9, 10], which has an overall accuracy of second order in time. Given a state vector of $\mathbf{a} = [\mathbf{u} \quad \rho \quad \Theta]^\top$, and horizontal and vertical forcings as $H(\mathbf{a})$ and $V(\mathbf{a})$ respectively, this scheme integrates the equations of motion over a time step Δt between time levels t^n and t^{n+1} as:

$$\mathbf{a}^1 = \mathbf{a}^n - \Delta t H(\mathbf{a}^n) \quad (45a)$$

$$\mathbf{a}^2 + \frac{\Delta t}{2} V(\mathbf{a}^2) = \mathbf{a}^n - \frac{\Delta t}{2} V(\mathbf{a}^n) - \frac{\Delta t}{2} H(\mathbf{a}^n) - \frac{\Delta t}{2} H(\mathbf{a}^1) \quad (45b)$$

$$\mathbf{a}^{n+1} + \frac{\Delta t}{2} V(\mathbf{a}^{n+1}) = \mathbf{a}^{n+1} - \frac{\Delta t}{2} V(\mathbf{a}^n) - \frac{\Delta t}{2} H(\mathbf{a}^n) - \frac{\Delta t}{2} H(\mathbf{a}^2). \quad (45c)$$

4.1. Implicit vertical solve

The errors at a given Newton iteration for the implicit vertical solver in (45) at nonlinear iteration, k may be expressed as residuals, drawing from (35) and (36) as

$$F_u = \mathbf{M}^{\mathcal{U}_\perp} \mathbf{u}^{\perp,k} - \mathbf{M}^{\mathcal{U}_\perp} \mathbf{u}^{\perp,n} + \Delta t \widehat{\mathbf{R}^{\perp,\parallel}} \mathbf{u}^\parallel + \Delta t (\mathbf{E}_\perp^{3,2})^\top \mathbf{M}^Q \overline{\Phi} + \Delta t \widehat{\mathbf{S}^{\mathcal{U}_\perp}} (\mathbf{M}^{\mathcal{U}_\perp})^{-1} (\mathbf{E}_\perp^{3,2})^\top \mathbf{M}^Q \overline{\Pi} \quad (46a)$$

$$F_\rho = \mathbf{M}^Q \rho^k + \mathbf{M}^Q \rho^n + \Delta t \mathbf{M}^Q \mathbf{E}_\perp^{3,2} \overline{\mathbf{U}}^\perp \quad (46b)$$

$$F_\Theta = \mathbf{M}^Q \Theta^k + \mathbf{M}^Q \Theta^n + \Delta t \mathbf{M}^Q \mathbf{E}_\perp^{3,2} (\mathbf{M}^{\mathcal{U}_\perp})^{-1} \widehat{\mathbf{S}^{\mathcal{U}_\perp}} \overline{\mathbf{U}}^\perp \quad (46c)$$

$$F_\Pi = \sum_{i=0}^{d_u-1} \left\langle \epsilon_j^Q, \log(\epsilon_i^Q \Pi_i^k) - \epsilon_i^Q \log\left(\frac{R}{c_v} \Theta_i^k\right) - \epsilon_i^Q \log(c_p) - \epsilon_i^Q \left(\frac{R}{c_v} \log\left(\frac{R}{p_0}\right)\right) \right\rangle_\Omega, \quad (46d)$$

where (46d) is the natural logarithm of the discrete equation of state (36d). The second order in time versions of the variational derivatives, (38), as introduced in (40) are given as [1, 3]

$$\mathbf{M}^{\mathcal{U}_\perp} \overline{\mathbf{U}}^\perp = \frac{1}{3} \mathbf{N}^{\mathcal{U}_{\perp,n}} \mathbf{u}^{\perp,n} + \frac{1}{6} \mathbf{N}^{\mathcal{U}_{\perp,n}} \mathbf{u}^{\perp,k} + \frac{1}{6} \mathbf{N}^{\mathcal{U}_{\perp,k}} \mathbf{u}^{\perp,n} + \frac{1}{3} \mathbf{N}^{\mathcal{U}_{\perp,k}} \mathbf{u}^{\perp,k} \quad (47a)$$

$$\mathbf{M}^Q \overline{\Phi} = \frac{1}{3} \mathbf{T}^{\mathcal{U}_{\perp,n}} \mathbf{u}^{\perp,n} + \frac{1}{3} \mathbf{T}^{\mathcal{U}_{\perp,k}} \mathbf{u}^{\perp,n} + \frac{1}{3} \mathbf{T}^{\mathcal{U}_{\perp,k}} \mathbf{u}^{\perp,k} + g (\mathbf{E}_\perp^{3,2})^\top \mathbf{M}^Q \mathbf{z} \quad (47b)$$

$$\mathbf{M}^Q \overline{\Pi} = \frac{1}{2} \mathbf{M}^Q \Pi^n + \frac{1}{2} \mathbf{M}^Q \Pi^k. \quad (47c)$$

At each Newton iteration, the updates to the solutions are computed from the approximate Jacobian, given as a 4×4 block system as

$$\begin{bmatrix} \mathbf{M}_u & \mathbf{0} & \mathbf{G}_\Theta & \mathbf{G}_\Pi \\ \mathbf{D}_\rho & \mathbf{M}_\rho & \mathbf{0} & \mathbf{0} \\ \mathbf{D}_\Theta & \mathbf{Q}_{\Theta,\rho} & \mathbf{M}_\Theta & \mathbf{0} \\ \mathbf{0} & \mathbf{0} & \mathbf{C}_\Theta & \mathbf{C}_\Pi \end{bmatrix} \begin{bmatrix} \delta \mathbf{u}^\perp \\ \delta \rho \\ \delta \Theta \\ \delta \Pi \end{bmatrix} \approx - \begin{bmatrix} F_u \\ F_\rho \\ F_\Theta \\ F_\Pi \end{bmatrix}, \quad (48)$$

where the blocks are defined as

$$\mathbf{M}_u = \mathbf{M}^{\mathcal{U}_\perp}, \quad (49a)$$

$$\mathbf{G}_\Theta = \frac{\Delta t}{2} \langle \epsilon_i^{\mathcal{U}_\perp} \cdot \widehat{\mathbf{p}}_h, \epsilon_j^Q \rangle \langle \epsilon_l^Q, \widehat{\rho}_h \epsilon_j^Q \rangle^{-1} \mathbf{M}^Q, \quad (49b)$$

$$\mathbf{G}_\Pi = \frac{\Delta t}{2} \widehat{\mathbf{S}^{\mathcal{U}_\perp}} (\mathbf{M}^{\mathcal{U}_\perp})^{-1} (\mathbf{E}_\perp^{3,2})^\top \mathbf{M}^Q, \quad (49c)$$

$$\mathbf{D}_\rho = \frac{\Delta t}{2} \mathbf{M}^Q \mathbf{E}_\perp^{3,2} (\mathbf{M}^{\mathcal{U}_\perp})^{-1} \widehat{\mathbf{N}^{\mathcal{U}_\perp}}, \quad (49d)$$

$$\mathbf{M}_\rho = \mathbf{M}^Q, \quad (49e)$$

$$\mathbf{D}_\Theta = \frac{\Delta t}{2} \mathbf{M}^Q \mathbf{E}_\perp^{3,2}, \quad (49f)$$

$$\mathbf{Q}_{\Theta,\rho} = \frac{\Delta t}{2} \langle \epsilon_i^Q, \epsilon_j^{\mathcal{U}_\perp} \cdot \widehat{\mathbf{u}}_{\perp,h} \rangle (\mathbf{M}^{\mathcal{U}_\perp})^{-1} (\mathbf{E}_\perp^{3,2})^\top \langle \epsilon_l^Q, \widehat{\theta}_h \epsilon_m^Q \rangle, \quad (49g)$$

$$\mathbf{M}_\Theta = \mathbf{M}^Q, \quad (49h)$$

$$\mathbf{C}_\Theta = -\frac{R}{c_v} \mathbf{M}^Q \langle \epsilon_i^Q, \Theta_j \epsilon_l^Q \rangle^{-1} \mathbf{M}^Q, \quad (49i)$$

$$\mathbf{C}_\Pi = \mathbf{M}^Q \langle \epsilon_i^Q, \Pi_j \epsilon_l^Q \rangle^{-1} \mathbf{M}^Q. \quad (49j)$$

Note that this approximate Jacobian is not, nor need it be, itself a skew-symmetric system such as the original system of residual vectors (46) in order to preserve energetic balances. All that is required is that this operator facilitate the convergence of such a system. The operators \mathbf{G}_Θ and $\mathbf{Q}_{\Theta,\rho}$ are of particular significance, since as will be seen these

allow for the Helmholtz structure of the reduced system. The operator $\mathbf{Q}_{\Theta,\rho}$ has the structure of the material advection term, which accounts for the fact that while the density advection equation (1b) is strictly a flux form equation, the density weighted potential temperature equation (1c) may equivalently be expressed as a material advection equation for the potential temperature [4, 12, 28].

In order to reduce (48) into a more computationally tractable form we begin by eliminating the density update as

$$\delta\rho = -\mathbf{M}_\rho^{-1}(\mathbf{F}_\rho + \mathbf{D}_\rho\delta\mathbf{u}) \quad (50)$$

Such that

$$\mathbf{D}_\Theta\delta\mathbf{u} - \mathbf{Q}_{\Theta,\rho}\mathbf{M}_\rho^{-1}(\mathbf{F}_\rho + \mathbf{D}_\rho\delta\mathbf{u}) + \mathbf{M}_\Theta\delta\Theta = -\mathbf{F}_\Theta \quad (51)$$

$$\begin{bmatrix} \mathbf{M}_u & \mathbf{G}_\Theta & \mathbf{G}_\Pi \\ \mathbf{D}_\Theta - \mathbf{Q}_{\Theta,\rho}\mathbf{M}_\rho^{-1}\mathbf{D}_\rho & \mathbf{M}_\Theta & \mathbf{0} \\ \mathbf{0} & \mathbf{C}_\Theta & \mathbf{C}_\Pi \end{bmatrix} \begin{bmatrix} \delta\mathbf{u} \\ \delta\Theta \\ \delta\Pi \end{bmatrix} = - \begin{bmatrix} \mathbf{F}_u \\ \mathbf{F}_\Theta - \mathbf{Q}_{\Theta,\rho}\mathbf{M}_\rho^{-1}\mathbf{F}_\rho \\ \mathbf{F}_\Pi \end{bmatrix} \quad (52)$$

Eliminating the Exner pressure update then gives

$$\delta\Pi = -\mathbf{C}_\Pi^{-1}(\mathbf{F}_\Pi + \mathbf{C}_\Theta\delta\Theta) \quad (53)$$

Such that

$$\mathbf{M}_u\delta\mathbf{u} + \mathbf{G}_\Theta\delta\Theta - \mathbf{G}_\Pi\mathbf{C}_\Pi^{-1}(\mathbf{F}_\Pi + \mathbf{C}_\Theta\delta\Theta) = -\mathbf{F}_u \quad (54)$$

$$\begin{bmatrix} \mathbf{M}_u & \mathbf{G}_\Theta - \mathbf{G}_\Pi\mathbf{C}_\Pi^{-1}\mathbf{C}_\Theta \\ \mathbf{D}_\Theta - \mathbf{Q}_{\Theta,\rho}\mathbf{M}_\rho^{-1}\mathbf{D}_\rho & \mathbf{M}_\Theta \end{bmatrix} \begin{bmatrix} \delta\mathbf{u} \\ \delta\Theta \end{bmatrix} = - \begin{bmatrix} \mathbf{F}_u - \mathbf{G}_\Pi\mathbf{C}_\Pi^{-1}\mathbf{F}_\Pi \\ \mathbf{F}_\Theta - \mathbf{Q}_{\Theta,\rho}\mathbf{M}_\rho^{-1}\mathbf{F}_\rho \end{bmatrix} \quad (55)$$

Finally, Schur complement reduction yields a single equation for the density weighted potential temperature update as

$$\begin{aligned} & \left[\mathbf{M}_\Theta - (\mathbf{D}_\Theta - \mathbf{Q}_{\Theta,\rho}\mathbf{M}_\rho^{-1}\mathbf{D}_\rho)\mathbf{M}_u^{-1}(\mathbf{G}_\Theta - \mathbf{G}_\Pi\mathbf{C}_\Pi^{-1}\mathbf{C}_\Theta) \right] \delta\Theta = \\ & - \left[\mathbf{F}_\Theta - \mathbf{Q}_{\Theta,\rho}\mathbf{M}_\rho^{-1}\mathbf{F}_\rho - (\mathbf{D}_\Theta - \mathbf{Q}_{\Theta,\rho}\mathbf{M}_\rho^{-1}\mathbf{D}_\rho)\mathbf{M}_u^{-1}(\mathbf{F}_u - \mathbf{G}_\Pi\mathbf{C}_\Pi^{-1}\mathbf{F}_\Pi) \right] \end{aligned} \quad (56)$$

Once (56) has been solved for the update to the density weighted potential temperature at nonlinear iteration k , the density, Exner pressure and velocity may be updated by (50), (53) and (54) respectively. Equation (56) has the structure of a Helmholtz equation, for which both the divergence, \mathbf{D}_Θ and gradient, \mathbf{G}_Θ terms are *corrected* by secondary terms due to the additional equations and dynamics. While the gradient correction will always be of the same sign as the original gradient due to the sign of (49i), it is at least theoretically possible that $\mathbf{Q}_{\Theta,\rho}$ could change sign. This could potentially result in multiple extrema and a catastrophic loss of convergence for the nonlinear system as a whole. However this has caused no problems in the tests performed here, and we are not sure of any physical scenarios in which this would be reversed.

4.2. Implementation details

The vertical integrator described in the preceeding section was implemented using the PETSc linear algebra library [29–31]. Since the solution variables for the vertical solve are all discontinuous across horizontal element boundaries, each horizontal element may be solved independently, which allows for dramatically increased computational performance. All matrix inverses detailed in the preceeding section may then be computed directly using LU decomposition, including the final solve for the density weighted potential temperature update (56).

In order to stabilise the model we add a biharmonic viscosity to both the horizontal momentum equation [17, 22], and the horizontal density weighted potential temperature equation, using a value of $0.072\Delta x^{3.2}$, where Δx is the average spacing between spectral element nodes. Additionally, the evaluation of horizontal and vertical fluxes of density and density weighted potential temperature at different time levels introduces a splitting error. While this error is negligible for non-hydrostatic resolutions due to the size of the time step, at planetary scales this splitting error results in additional vertical oscillations. As such we introduce a Rayleigh damping term [32] to vertical momentum equation in the top three levels, with descending values of $4.0/\Delta t$, $2.0/\Delta t$, $1.0/\Delta t$. Note that this term is applied only to the first test case described below.

5. Results

5.1. Baroclinic instability

We validate the model using a z -level dry baroclinic instability test case [33] with the shallow atmosphere approximation. The initial state is one of geostrophic horizontal and hydrostatic vertical balance, overlaid with a small, $O(1\text{m/s})$, perturbation to the zonal and meridional velocity components. The model was run with 24×24 elements of degree $p = 3$ on each face of the cubed sphere (and piecewise constant/linear elements in the vertical), for an averaged resolution of $\Delta x \approx 128\text{km}$ and 30 vertical levels on 96 processors with a time step of $\Delta t = 120\text{s}$.

Figures 1 and 2 show the zonal averages of density ρ , Exner pressure Π , potential temperature θ and zonal velocity u at day 10 (solid lines), as well as the differences between the final and initial states. These profiles show little difference between the initial and final states, with the exception of the zonal velocity, which exhibits a small kink near the bottom boundary where the baroclinic instability occurs, demonstrating that the leading order geostrophic and hydrostatic balances in the horizontal and vertical are well satisfied.

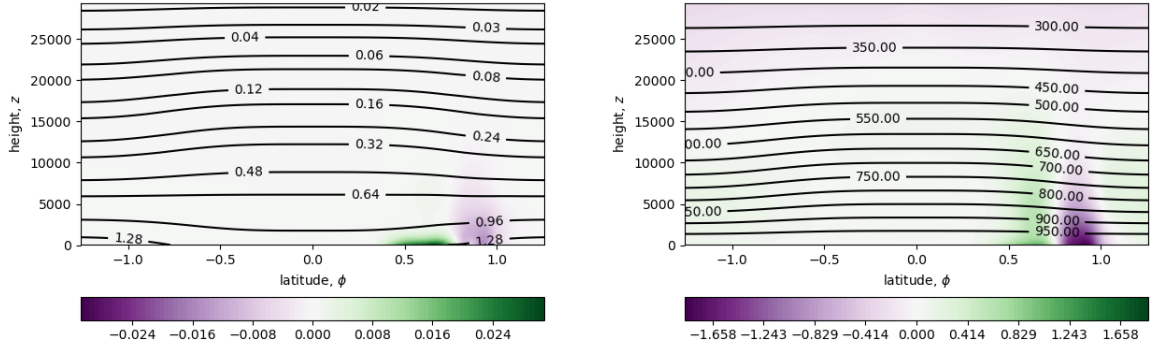


Figure 1: Zonal averages of density, ρ_h in $\text{kg} \cdot \text{m}^{-3}$ (left) and Exner pressure, Π_h in $\text{m}^2 \text{s}^{-2} \text{K}^{-1}$ (right) at day 10. Contours represent absolute values, and shades represent differences from initial values.

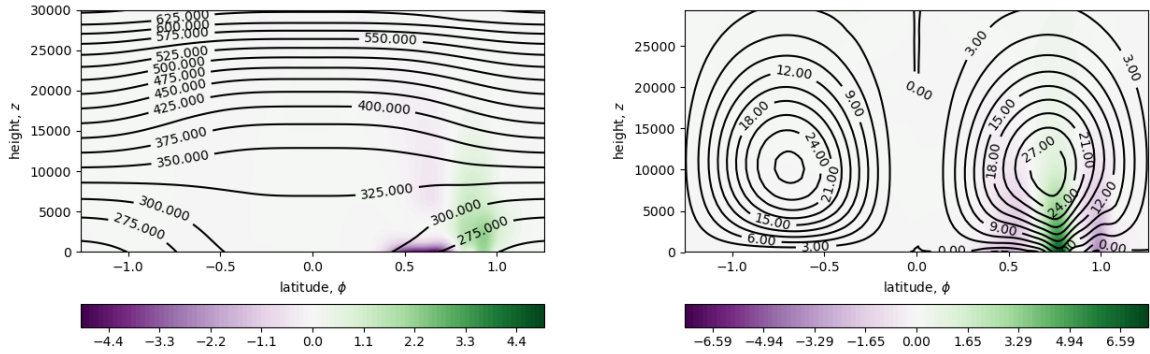


Figure 2: Zonal averages of potential temperature, θ_h in K (left) and zonal velocity, u_h in $\text{m} \cdot \text{s}^{-1}$ (right) at day 10. Contours represent absolute values, and shades represent differences from initial values.

Figure 3 shows the evolution of the potential, internal and kinetic (horizontal and vertical) energy with time. As can be seen the advent of the baroclinic instability coincides with a loss of both potential and internal energy, and an increase of kinetic energy due to acceleration in both the horizontal and vertical directions. The signature of the internal gravity waves is also visible in the smaller scale oscillation of the potential and horizontal kinetic energies. The high frequency oscillation in the vertical kinetic energy is due to the splitting error associated with the evaluation of horizontal and vertical fluxes at different time levels within the HEVI scheme. Note that the total amounts of potential and internal energy are approximately 3.6×10^{23} and $9.2 \times 10^{23} \text{ kg} \cdot \text{m}^2 \text{s}^{-2}$ respectively, and so are several orders of magnitude greater than the amounts of horizontal and vertical kinetic energy (approximately 4.0×10^{20} and $3.0 \times 10^{13} \text{ kg} \cdot \text{m}^2 \text{s}^{-2}$ respectively). As such the flattening of the density contours from which the baroclinic instability draws energy are barely evident in Fig. 1.

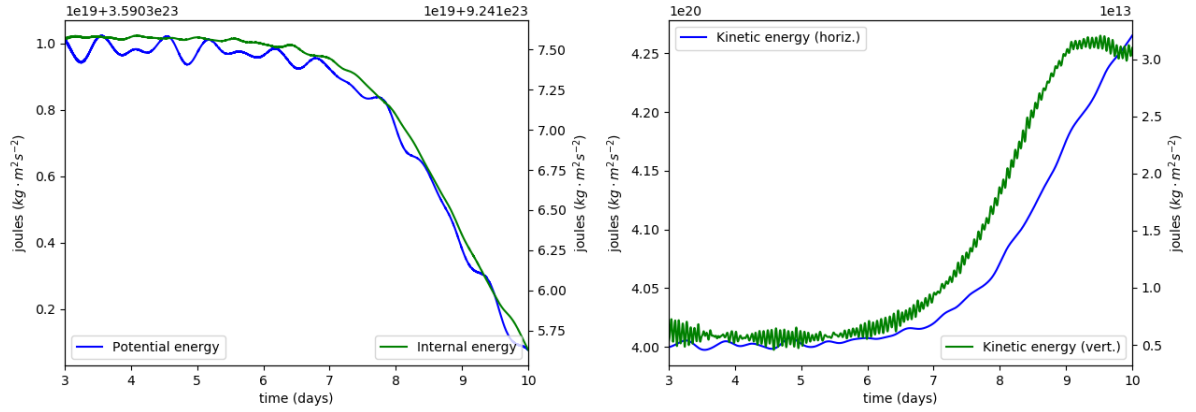


Figure 3: Left: time evolution of the potential and internal energies. Right: time evolution of the kinetic energy (horizontal and vertical).

Figure 4 shows the power exchanges between kinetic, potential and internal energy, as given in (42)-(44). The evolution of the baroclinic instability is evident in the increase of power associated with the internal to horizontal kinetic energy exchanges. This figure also shows the typical convergence of the iterative solver with Newton iteration (taken at day 9). As can be seen, the convergence is poor for the first couple of Newton iterations, and the convergence of the velocity lags the other variables. After the first couple of iterations, the convergence improves, and reduces the errors between one and two decades at each iteration. Note that as the Jacobian is only approximate, we do not anticipate the convergence to be strictly quadratic. Also note that this convergence plot shows the convergence for the column of elements with the largest error, which may not necessarily be the same column between Newton iterations.

The bottom level Exner pressure Π , potential temperature, θ , and the vertical component of the relative vorticity, ω are presented for $z \approx 1.5 \text{ km}$ at days 8 and 10 in Figs. 5, 6 and 7. The meridional cross section of the pressure perturbation at 50°N in Fig. 8. In the cases of the pressure, this is reconstructed from the model variables as $p = p_0(\Pi/c_p)^{c_p/R}$. The pressure perturbation in Fig. 8 is then derived by removing the average pressure at the corresponding vertical level at 50°S . These results compare well with the previously published test case results [33], and the vertical pressure perturbation profile exhibits less noise than the previous version of the implicit solver [8].

In order to validate the conservation properties of the implicit solver the horizontal dynamics were turned off and the model was re-run with only the implicit vertical solver active (such that the horizontal velocity was not updated between time steps), and all the dissipation terms removed. Note that while the horizontal scheme conserves mass [8], it does not conserve energy due to the explicit time integration. As shown in Fig. 9 while the mass is conserved to machine precision, there is a small loss of total energy over time. This is most likely due to either the finite tolerance of the implicit solver, or to round off errors due to the use of physical units, for which the vertical kinetic energy is approximately ten orders of magnitude smaller than either the potential or internal energies.

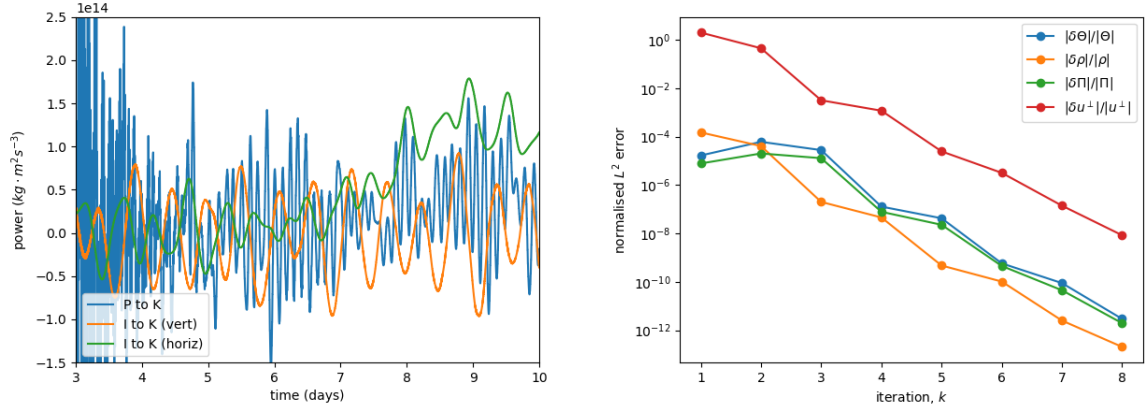


Figure 4: Left: power associated with energetic exchanges, days 3 to 10. Right: typical convergence of the normalised L^2 magnitude of the solution updates with Newton iteration (taken at day 9).

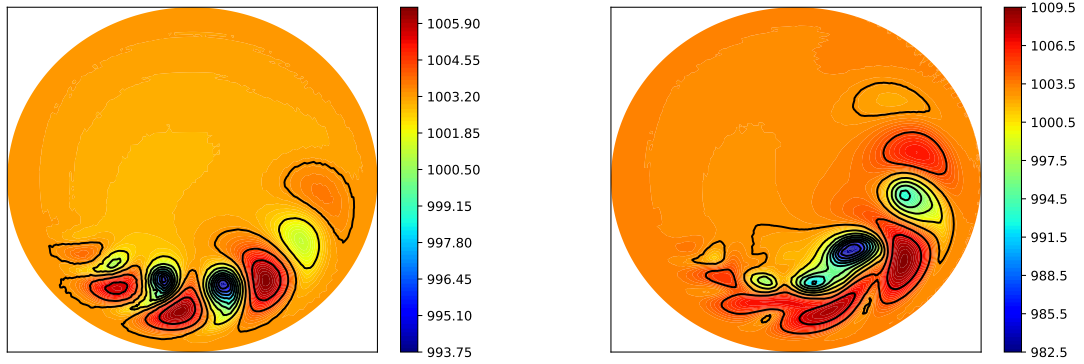


Figure 5: Bottom level Exner pressure, Π_h (in hPa) day 8 (left) and 10 (right).

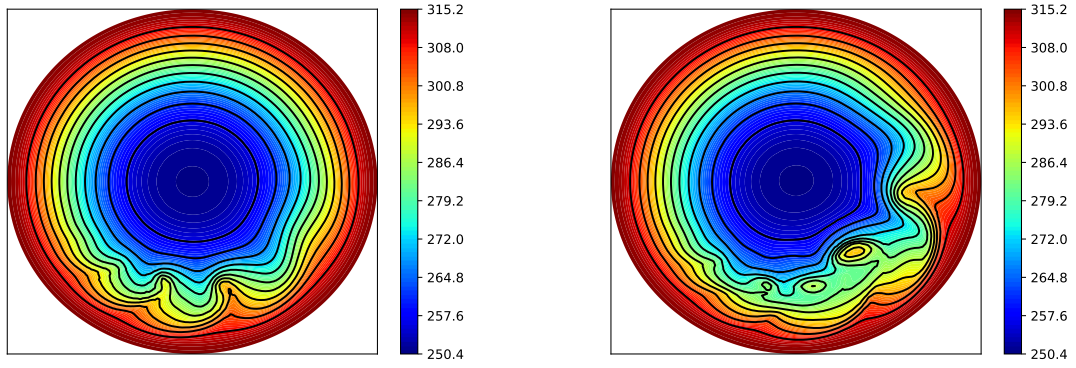


Figure 6: Potential temperature, θ_h (in $^{\circ}\text{K}$) at $z \approx 1.5\text{km}$, day 8 (left) and 10 (right).

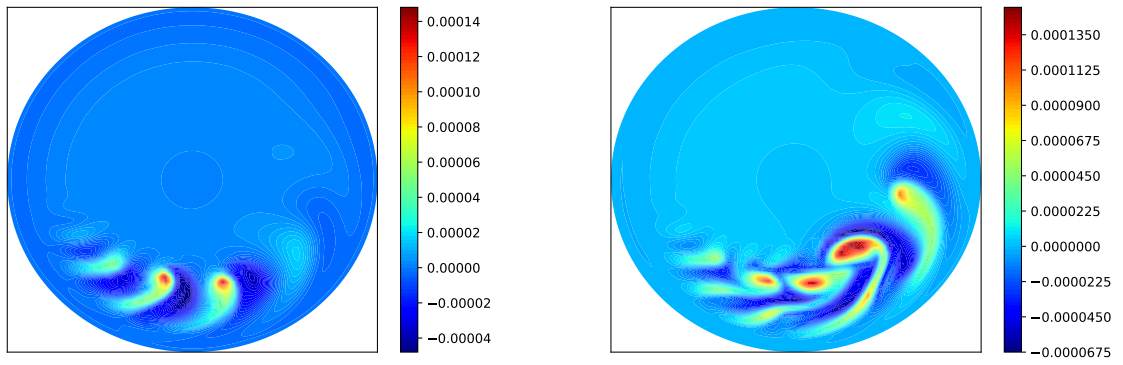


Figure 7: Vertical component of the relative vorticity, ω_h (in s^{-1}) at $z \approx 1.5\text{km}$, day 8 (left) and 10 (right).

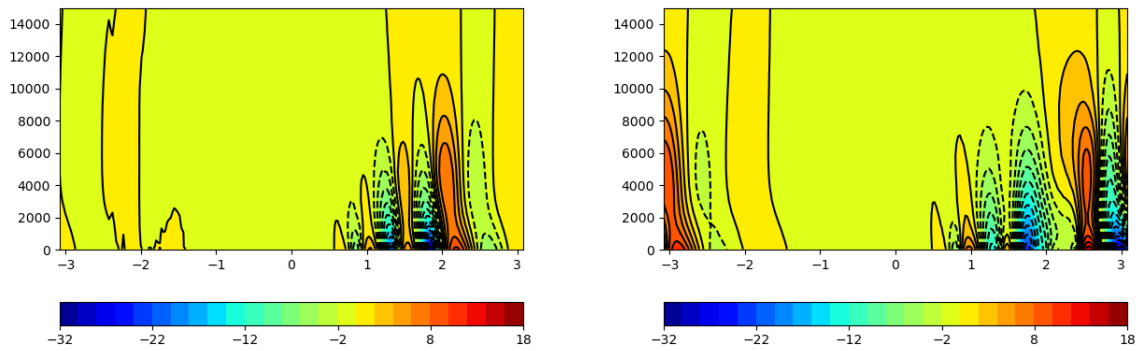


Figure 8: Vertical cross section of the pressure perturbation, $p_h - \bar{p}_h$ (in hPa) at 50°N , day 8 (left) and day 10 (right).

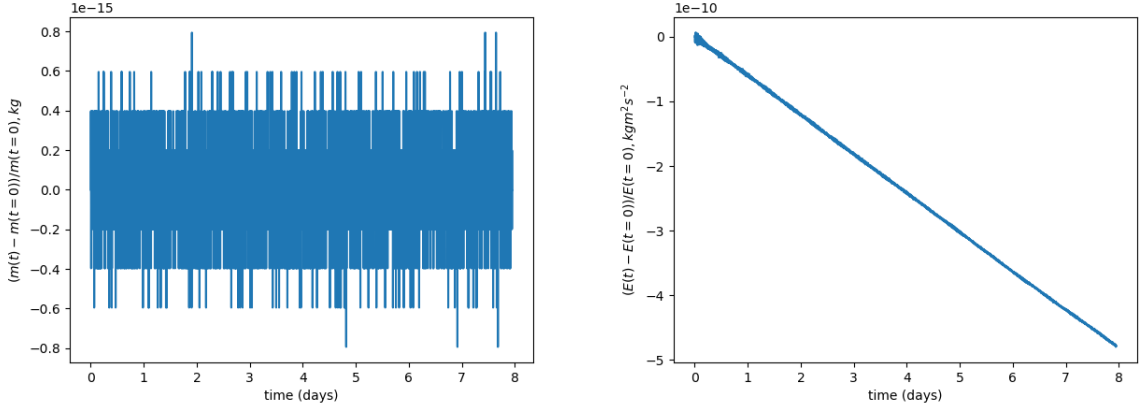


Figure 9: Global conservation errors for mass (left) and total energy (right), vertical dynamics only.

5.2. Non-hydrostatic gravity wave

In order to validate the vertical integrator at high resolutions at which non-hydrostatic dynamics become significant the model has also been tested for the propagation of a non-hydrostatic gravity wave driven by a potential temperature perturbation on a planet with a reduced radius 125 times smaller than that of the earth. This test was originally proposed as part of the 2012 DCMIP workshop [34], and specific details of the initial configuration can be found within the DCMIP test case document on the web site.

As for the baroclinic instability test, the simulation was run with a resolution of 24×24 elements of degree $p = 3$ in each cubed sphere panel. We use 16 evenly spaced vertical levels over a total height of 10,000.0m, and a time step of $\Delta t = 0.5$ s for a total simulation time of 3600s. In order to account for the highly oscillatory nature of the dynamics the horizontal biharmonic viscosity was rescaled by a factor of 2.0 for both the momentum and temperature equations for a value of $0.144\Delta x^{3.2}$.

This test case is especially challenging for the higher order spectral element spatial discretisation, firstly since we have not applied any sort of upwinding or monotonicity preservation method to either the continuity or temperature equation, and secondly because the temperature equation is cast as a flux form equation for the density weighted potential temperature, $\Theta = \rho\theta$, from which the potential temperature, θ , is then diagnosed. This is in contrast to a material form of the potential temperature advection, in which upwinding may be directly applied in the flux reconstruction [12], or by re-weighting the test function in an energetically consistent manner [4].

Figure 10 shows the longitude-height equatorial ($\phi = 0^\circ$) cross section of the potential temperature perturbation, $\theta'(\lambda, 0, z) = \theta(\lambda, 0, z) - \bar{\theta}(z)$, where $\bar{\theta}(z)$ is the mean potential temperature at a given height, after 30 minutes and 1 hour. While the structure and evolution of the perturbation qualitatively match the results presented for other non-hydrostatic models, the absence of a monotone upwinded advection scheme means that our results are slightly more oscillatory than those of other models. Moreover our results also show the ejection of a small hot bubble which rises to the top of the domain, which is also most likely an artefact of our non-monotone scheme.

The energy partitions are given for the final 12 minutes of the simulation in Fig. 11. The signature of the internal gravity wave is clearly visible in the oscillation between potential and internal energy. The horizontal dynamics are also observed in the longer time scale oscillation of kinetic to internal energy exchanges. This is also observed in the power exchanges as given in Fig. 12.

Figure 12 also shows nonlinear convergence of the vertical solver at time $t = 1$ hour. Due to the more regular vertical structure than the baroclinic test case the convergence of the nonlinear solver is faster and more regular, taking just 4 iterations compared to the 8 required for the baroclinic instability test case as seen in Fig. 4.

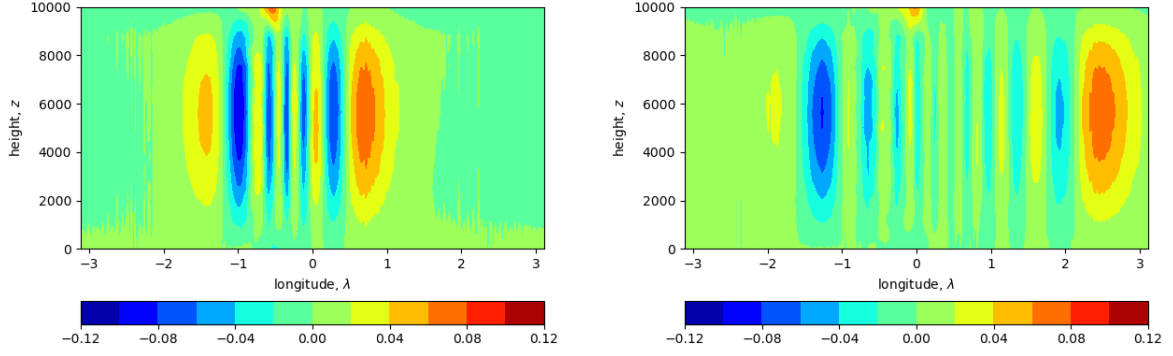


Figure 10: Longitude-height equatorial ($\phi = 0^\circ$) cross section of the potential temperature perturbation, $\theta'(\lambda, 0, z) = \theta(\lambda, 0, z) - \bar{\theta}(z)$ at times $t = 30$ minutes (left) and $t = 60$ minutes (right).

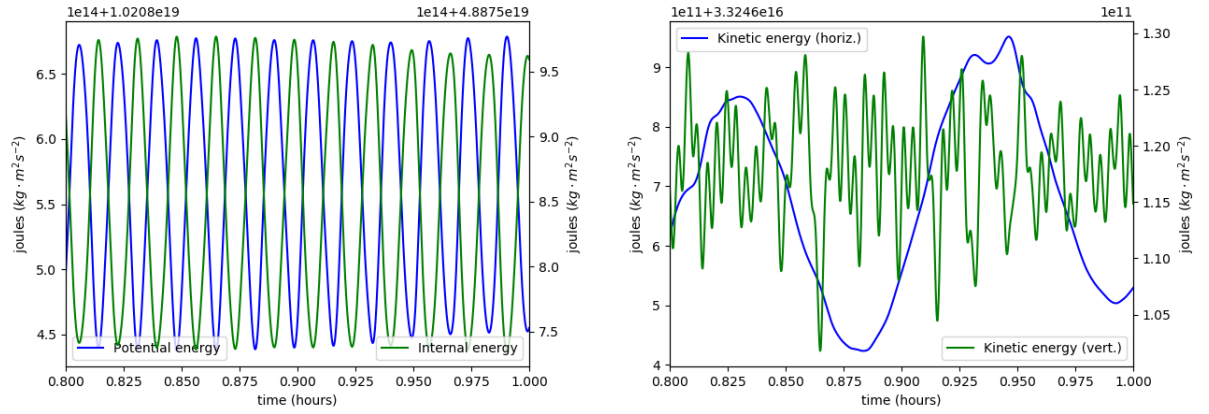


Figure 11: Internal gravity wave; left: time evolution of the potential and internal energies, right: time evolution of the kinetic energy (horizontal and vertical).

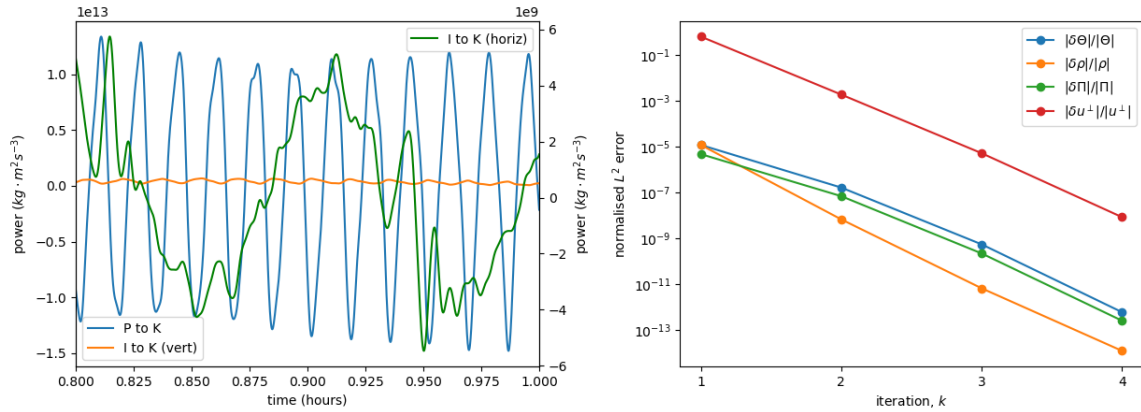


Figure 12: Left: power associated with energetic exchanges, days 3 to 10. Right: typical convergence of the normalised L^2 magnitude of the solution updates with Newton iteration (at 1 hour).

6. Conclusions

An energetically balanced time integrator for vertical atmospheric dynamics is presented. The integrator balances energetic exchanges associated with vertical motions by preserving the skew-symmetric property of the non-canonical Hamiltonian form of the compressible Euler equations in space and time. The computational efficiency of the integrator is accelerated via a reduction of the four component system to a single equation for the density weighted potential temperature at each nonlinear iteration. The integrator is implemented within the context of a horizontally explicit/vertically implicit scheme in which the vertical time stepping is centered so as to allow for second order accuracy and exact integration in time. The integrator demonstrates robust convergence at both global and non-hydrostatic resolutions.

In future work the issue of the time splitting error associated with the density and density weighted potential temperature fluxes will be addressed. These can most likely be reformulated so as to suppress this error and ensure consistency between time levels. Fully three dimensional versions of the implicit integrator will also be investigated.

7. Acknowledgments

David Lee would like to thank Drs. Marcus Thatcher and John McGregor for their continued support and access to computing resources. This project was supported by resources and expertise provided by CSIRO IMT Scientific Computing.

References

- [1] W. Bauer, C. J. Cotter, Energy-entropy conserving compatible finite element schemes for the rotating shallow water equations with slip boundary conditions, *J. Comp. Phys.* 373 (2018) 171–187.
- [2] C. Eldred, T. Dubos, E. Kritsikis, A quasi-Hamiltonian discretization of the thermal shallow water equations, *J. Comp. Phys.* 379 (2019) 1–31.
- [3] G. A. Wimmer, C.J. Cotter, W. Bauer, Energy conserving upwinded compatible finite element schemes for the rotating shallow water equations, *J. Comp. Phys.* 401 (2020) 109016
- [4] G. A. Wimmer, C.J. Cotter, W. Bauer, Energy conserving SUPG methods for compatible finite element schemes in numerical weather prediction, *arXiv:2001.09590* (2020)
- [5] K. Kormann, E. Sonnendrücker, Energy-conserving time propagation for a geometric particle-in-cell VlasovMaxwell solver, *arXiv:1910.04000* (2019)
- [6] R. I. McLachlan, G. R. W. Quispel, N. Robidoux, Geometric integration using discrete gradients, *Phil. Trans. R. Soc. A* 357 (1999) 10211046.
- [7] D. Cohen, E. Hairer, Linear energy-preserving integrators for Poisson systems, *BIT Numer. Math.* 51 (1) (2011) 91101.
- [8] D. Lee, A. Palha, A mixed mimetic spectral element model of the 3D compressible Euler equations on the cubed sphere, *J. Comp. Phys.* 401 (2020) 108993

- [9] H. Weller, S. J. Lock, N. Wood, RungeKutta IMEX schemes for the Horizontally Explicit/Vertically Implicit (HEVI) solution of the wave equations, *J. Comp. Phys.* 252 (2013) 365–381.
- [10] S.-J. Lock, N. Wood, H. Weller, Numerical analyses of RungeKutta implicitexplicit schemes for horizontally explicit, vertically implicit solutions of atmospheric models, *Q. J. R. Meteorol. Soc.* 140 (2014) 1654–1669.
- [11] M. A. Taylor, O. Guba, A. Steyer, P. A. Ullrich, D. M. Hall, C. Eldred, An Energy Consistent Discretization of the Nonhydrostatic Equations in Primitive Variables, *JAMES*, 12 (2020) 1–20.
- [12] T. Melvin, T. Benacchio, B. Shipway, N. Wood, J. Thuburn, C. Cotter, A mixed finite-element, finite-volume, semi-implicit discretisation for atmospheric dynamics: Cartesian geometry, *Q. J. R. Meteorol. Soc.* (2019) 1–19.
- [13] C. Maynard, T. Melvin, E. H. Müller, Performance of multigrid solvers for the mixed finite element dynamical core LFRic, arXiv:2002.00756, (2020)
- [14] M. Gerritsma, Edge functions for spectral element methods, in: *Spectral and high order methods for partial differential equations*, Lecture Notes in Computational Science and Engineering, Springer 76 (2011) 199–207.
- [15] J. Kreeft, M. Gerritsma, Mixed mimetic spectral element method for Stokes flow: A pointwise divergence-free solution, *J. Comp. Phys.* 240 (2013) 284–309.
- [16] D. Lee, A. Palha, M. Gerritsma, Discrete conservation properties for shallow water flows using mixed mimetic spectral elements, *J. Comp. Phys.* 357 (2018) 282–304.
- [17] D. Lee, A. Palha, A mixed mimetic spectral element model of the rotating shallow water equations on the cubed sphere, *J. Comp. Phys.* 375 (2018) 240–262.
- [18] P. Névir, M. Sommer, Energy-vorticity theory of ideal fluid mechanics, *J. Atmos. Sci.* 66 (2009) 2073–2084.
- [19] A. Gassmann, A global hexagonal Cgrid nonhydrostatic dynamical core (ICONIAP) designed for energetic consistency, *Q. J. R. Meteorol. Soc.* 139 (2013) 152–175.
- [20] A. A. White, B. J. Hoskins, I. Roulstone, A. Staniforth, Consistent approximate models of the global atmosphere: shallow, deep, hydrostatic, quasi-hydrostatic and non-hydrostatic, *Q. J. R. Meteorol. Soc.* 131 (2005) 2081–2107.
- [21] E. Hairer, C. Lubich, G. Wanner, *Geometric Numerical Integration*, Springer, 2006.
- [22] O. Guba, M. A. Taylor, P. A. Ullrich, J. R. Overfelt, M. N. Levy, The spectral element method (SEM) on variable-resolution grids: evaluating grid sensitivity and resolution-aware numerical viscosity, *Geosci. Model. Dev.* 7 (2014) 2803–2816.
- [23] E. Celledoni, V. Grimm, R. I. McLachlan, D. I. McLaren, D. O’Neale, B. Owren, G. R. W. Quispel, Preserving energy resp. dissipation in numerical PDEs using the “average vector field” method, *J. Comp. Phys.* 231 (2012) 6770–6789.
- [24] P. Ullrich, C. Jablonowski, Operator-split RungeKuttaRosenbrock methods for nonhydrostatic atmospheric models, *Mon. Wea. Rev.* 140 (2012) 1257–1284.
- [25] F. X. Giraldo, J. F. Kelly, E. M. Constantinescu, Implicit-explicit formulations of a three-dimensional nonhydrostatic unified model of the atmosphere (NUMA), *SIAM J. Sci. Comput.* 35 (2013) B1162–B1194.
- [26] L. Bao, R. Klöforn, R. D. Nair, Horizontally explicit and vertically implicit (HEVI) time discretization scheme for a discontinuous Galerkin nonhydrostatic model, *Mon. Wea. Rev.* 143 (2015) 972–990.
- [27] D. J. Gardner, J. E. Guerra, F. P. Hamon, D. R. Reynolds, P. A. Ullrich, C. S. Woodward, Implicit-explicit (IMEX) Runge-Kutta methods for non-hydrostatic atmospheric models, *Geosci. Model Dev.* 11 (2018) 1497–1515.
- [28] A. Natale, J. Shipton, C. J. Cotter, Compatible finite element spaces for geophysical fluid dynamics, *Dyn. Stat. Climate Sys.* 1 (2016) 1–31.
- [29] S. Balay, S. Abhyankar, M. F. Adams, J. Brown, P. Brune, K. Buschelman, L. Dalcin, V. Eijkhout, W. D. Gropp, D. Kaushik, M. G. Knepley, D. A. May, L. C. McInnes, K. Rupp, B. F. Smith, S. Zampini, H. Zhang, PETSc Web page, <http://www.mcs.anl.gov/petsc> (2017).
- [30] S. Balay, S. Abhyankar, M. F. Adams, J. Brown, P. Brune, K. Buschelman, L. Dalcin, V. Eijkhout, W. D. Gropp, D. Kaushik, M. G. Knepley, D. A. May, L. C. McInnes, K. Rupp, P. Sanan, B. F. Smith, S. Zampini, H. Zhang, PETSc users manual, Tech. Rep. ANL-95/11 - Revision 3.8, Argonne National Laboratory (2017).
- [31] S. Balay, W. D. Gropp, L. C. McInnes, B. F. Smith, Efficient management of parallelism in object oriented numerical software libraries, in: E. Arge, A. M. Bruaset, H. P. Langtangen (Eds.), *Modern Software Tools in Scientific Computing*, Birkhäuser Press, 1997, pp. 163–202.
- [32] J. B. Klemp, J. Dudhia, A. D. Hassiotis, An upper gravity-wave absorbing layer for NWP applications, *Mon. Wea. Rev.* 136 (2008) 3987–4004.
- [33] P. A. Ullrich, T. Melvin, C. Jablonowski, A. Staniforth, A proposed baroclinic wave test case for deep and shallowatmosphere dynamical cores, *Q. J. R. Meteorol. Soc.* 140 (2014) 1590–1602.
- [34] C. Jablonowski, P. A. Ullrich, J. Kent, K. Reed, M. A. Taylor, P. H. Lauritzen, R. D. Nair, DCMIP 2012 test case 3.1, https://www.earthsystemcog.org/projects/dcmip-2012/test_cases (2012).